Dong et al. *NPG Asia Materials* (2023) 15:47
https://doi.org/10.1038/s41427-023-00494-9

NPG Asia Materials

ARTICLE Open Access

Ultrafine-bubble-water-promoted nanoceramic decoration of metal powders for additive manufacturing

Mingqi Dong[1], Weiwei Zhou[1], Suxia Guo[1] and Naoyuki Nomura[1]

Abstract

The design of composite powders for exploiting the multifunctionality of metallic nanocomposites via laser additive manufacturing (AM) is challenging. Conventional ball-milling processes are prone to cause uncontrollable powder morphology and reduced flowability, while recently developed nanodecoration technologies are limited by complicated processing and impurity inclusion. Herein, a facile and scalable approach was developed using ultrafine bubble (UFB)-assisted heteroagglomeration to fabricate high-concentration, impurity-free nanoceramic/metal composite powders. Individual ZrO_2 or Al_2O_3 nanoparticles up to ~10 wt% were homogeneously decorated on the surface of Ti-6Al-4V powders through the bridging effect of the negatively charged UFBs, leading to enhanced flowability and laser absorptivity. The nanoceramics were completely decomposed and dissolved into the matrix upon laser irradiation; therefore, a unique Ti nanocomposite exhibiting both high strength and ductility was obtained. Our work provides new insights into the application of UFBs and the fabrication of multifunctional AM components.

Introduction

Structural metallic materials are the cornerstone of industrial society[1,2]. High-performance metallic components are extensively used in extreme environments. Therefore, these components usually require complex structures with a combination of properties, such as high strength–ductility synergy, good wear resistance, high thermal stability, and reliability[2]. Laser powder bed fusion (L-PBF), additive manufacturing (AM) technology, has been a key technology for material innovation and design[3]. Although the L-PBF process is effective for metallic component fabrication, AM products have limited properties, because of which they cannot meet the requirements for state-of-the-art industrial applications[4].

Nanoparticle dispersion has emerged as an effective approach to mechanically functionalize metallic materials[5]. In the past decade, fillers such as ceramics (e.g., SiC[5,6], TiC[7], TiB[8], B_4C[9], Al_2O_3[10], and ZrO_2[11]) and nanocarbons[12] have been utilized to strengthen metallic components through AM. However, AM composite powders are mostly prepared by ball milling processes[13]. Nanoparticles easily agglomerate under strong van der Waals forces during low-energy ball milling[14], while the powders prepared by high-energy ball milling may undergo crushing or tangling and possess poor flowability[15], which severely weakens the comprehensive properties of the final products[16,17]. Recently, some attempts have been devoted to the decoration of metallic powders with high-concentration nanofillers without sacrificing flowability. For instance, carbon nanotubes (CNTs) were planted in situ on a Ti alloy powder surface using a C_2H_2 gaseous precursor and a solid-solution Fe catalyst via fluidized bed chemical vapor deposition. The mixed powders displayed spherical morphology and good CNT dispersion, thereby exhibiting good AM processability[18]. Lin et al.[19] also demonstrated that uniformly dispersed TiC nanoparticle/Al powders could be obtained in molten salt with ultrasonication. The composite powders showed a near-spherical shape with enhanced laser absorption, facilitating the AM

Correspondence: Weiwei Zhou (weiwei.zhou.c3@tohoku.ac.jp) or Naoyuki Nomura (naoyuki.nomura.a2@tohoku.ac.jp)
[1]Department of Materials Processing, Graduate School of Engineering, Tohoku University, Sendai 980-8579, Japan

fabrication of ultrahigh-strength Al composites. Moreover, CNTs were utilized as a bridging agent to produce high-concentration nano-Al_2O_3/Mo alloy powders via hetero-agglomeration[17]. Although the abovementioned strategies are promising, their applications are limited because of complicated processing and the unavoidable inclusion of impurities. Furthermore, the types of nanofillers are restricted because intrinsically characteristic properties, such as chemical, thermal stability, and melting points, are required for raw powder materials. Thus, a novel approach is required that promotes nanoparticle dispersion while retaining the original features of metallic powders.

Ultrafine bubbles (UFBs) are gaseous domains that typically range from tens to hundreds of nanometers in size, possessing high stability and longevity in deionized water[20]. The adsorption of the OH^- group is dominant at the water–bubble interface induced by the difference in the enthalpy of hydration between H^+ and OH^- ions, resulting in the formation of negatively charged surfaces of UFBs[21]. Thus, UFBs could bridge two positively charged species without the formation of residues during heteroagglomeration. Although UFB water is presently used in various fields, such as environmental remediation, medicine, and fluidics, its underlying potential in materials science has not yet been realized.

Herein, UFB-assisted heteroagglomeration (UFBH) is proposed for composite powder fabrication. The feasibility of fabricating high-concentration, impurity-free nanoceramic/metal composite powders was initially demonstrated using UFB water. ZrO_2 and Al_2O_3 nanoceramics were introduced as reinforcement particles due to their excellent physical and mechanical properties, such as low density, high hardness, and high fracture strength. Moreover, under high-energy laser irradiation and rapid solidification during L-PBF, these nanoparticles may partially melt, forming favorable interface bonding with the Ti matrix or providing excellent solid-solution strengthening.

In addition to their spherical morphology, the nanoceramic-decorated Ti–6Al–4V (Ti64) powders exhibited enhanced flowability and laser absorptivity. Consequently, the AM-produced Ti64 composite exhibited a unique and superior combination of high tensile strength and high ductility owing to significant solid solution strengthening and grain refinement. This study introduces a facile and scalable approach using UFBH and laser AM processes to design multifunctional metallic components.

Results and discussion

Characteristics of raw powders and UFB water

In this work, ZrO_2 and Al_2O_3 nanoparticles and Ti64 alloy powders were selected to study the UFBH process. Figure 1a displays the spherical morphology of the raw Ti64 alloy powders via field emission scanning electron microscopy (FESEM). As shown by the cross-sectional transmission electron microscopy (TEM) image and corresponding selected-area electron diffraction (SAED) pattern of a Ti64 particle in Fig. 1b, this alloy possessed twinning structures, which corresponded to α′-Ti martensite induced by high-speed cooling during the gas-atomization process. Moreover, close-up energy dispersive X-ray spectroscopy (EDXS) and high-resolution TEM (HRTEM) showed the presence of a 6-nm-thick amorphous oxide film coated on the surface of the Ti64 particle (Fig. 1c, d). These oxide scales preferentially adsorb H^+ ions, thereby imparting a positive surface charge to metal powders in water[22]. The untreated ZrO_2 and Al_2O_3 nanoceramic particles showed near-spherical shapes, displaying average approximate diameters of 53 and 125 nm, respectively (Fig. 1e, f). The zeta potentials of ZrO_2 and Al_2O_3 in deionized water were measured as +18 mV and +49 mV, respectively (Fig. S1). Because both the alloy powder and ceramic nanoparticles exhibited the same positive charge, no electrostatic attraction was expected between Ti64 and ZrO_2 or Al_2O_3 nanoparticles in the aqueous suspension.

Because of the nanodimensional, homogeneous characteristics of UFBs in water, the Tyndall phenomenon was analyzed for their detection. Figure 2a, b shows a laser beam passing through the deionized and UFB water, respectively. The laser path was clearly observed in the UFB water due to UFB-induced light scattering. A snapshot of the light scattered by UFBs was obtained through high-magnification optical microscopy (Fig. 2c). The concentration of UFBs was determined to be $1.76 \times 10^8 \pm 1.48 \times 10^7$ mL^{-1}.

The UFB water exhibited a negative zeta potential of −18.4 mV (Fig. S1), attributed to the adsorption of the OH^- group on the UFB surface[20]. To elucidate the bridging ability of UFBs during powder mixing, a 5 wt% ZrO_2/Ti64 suspension was individually prepared in deionized and UFB water by heteroagglomeration. In the deionized-water-based suspension, the supernatant ZrO_2 nanoparticles remained dispersed after a settling time of 5 h, while the Ti64 powders quickly sedimented on the bottom of the beaker owing to gravity and their weak surface charge (Fig. 2d). In the UFB-water-based suspension, the supernatant became completely transparent after settling for only 0.5 h (Fig. 2e). This confirmed that UFBs promoted the adsorption of ceramic nanoparticles onto the Ti64 powder surfaces.

Morphologies of nanoceramic/Ti64 powders

The observed morphology of ZrO_2/Ti64 or Al_2O_3/Ti64 powders produced by the UFBH process is illustrated in Fig. 3 and Fig. S2. Individual ZrO_2 nanoparticles were uniformly decorated on the Ti64 powder surface at 1 wt% (Fig. 3a) and became more visible with increasing ZrO_2 content (i.e., 5 wt% ZrO_2; Fig. 3b). The entire surface of

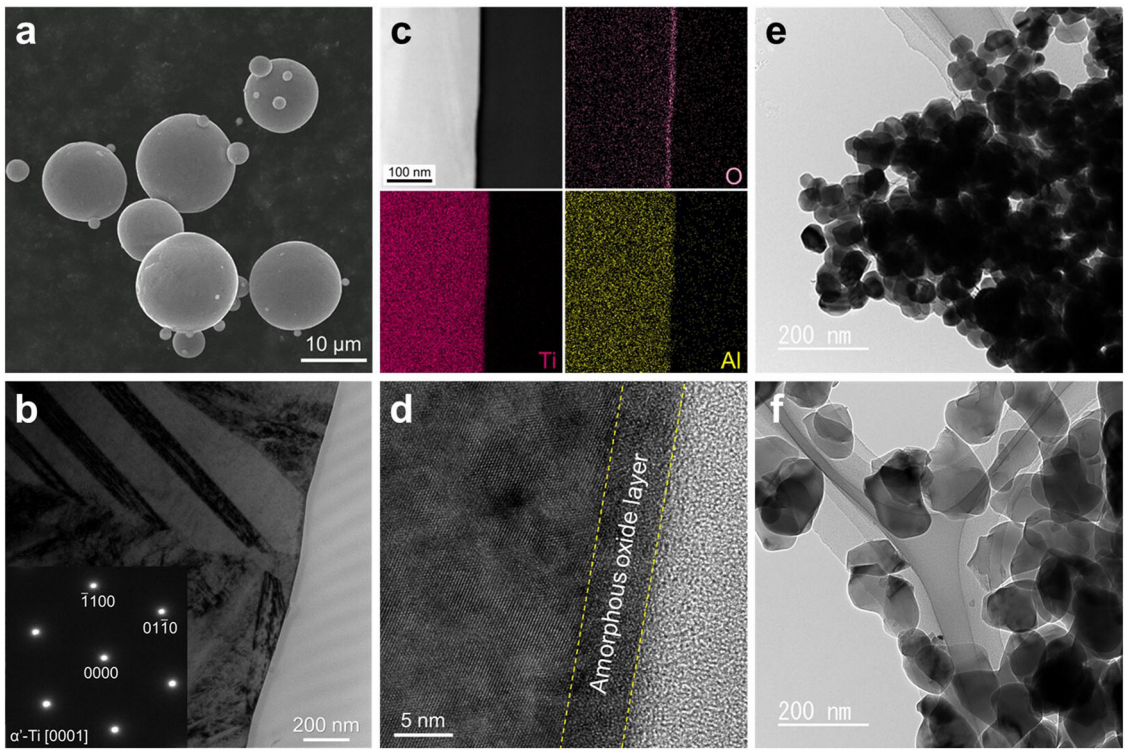

Fig. 1 Microstructures of raw materials used in this work. a FESEM, **b** TEM, and **d** HRTEM images of the Ti64 powders; inset in **b** shows the SAED pattern of α′-Ti. **c** Scanning transmission electron microscopy (STEM) image and the corresponding EDXS mappings of a cross-sectional Ti64 particle near the powder surface; TEM images of the **e** ZrO_2 and **f** Al_2O_3 nanoparticles.

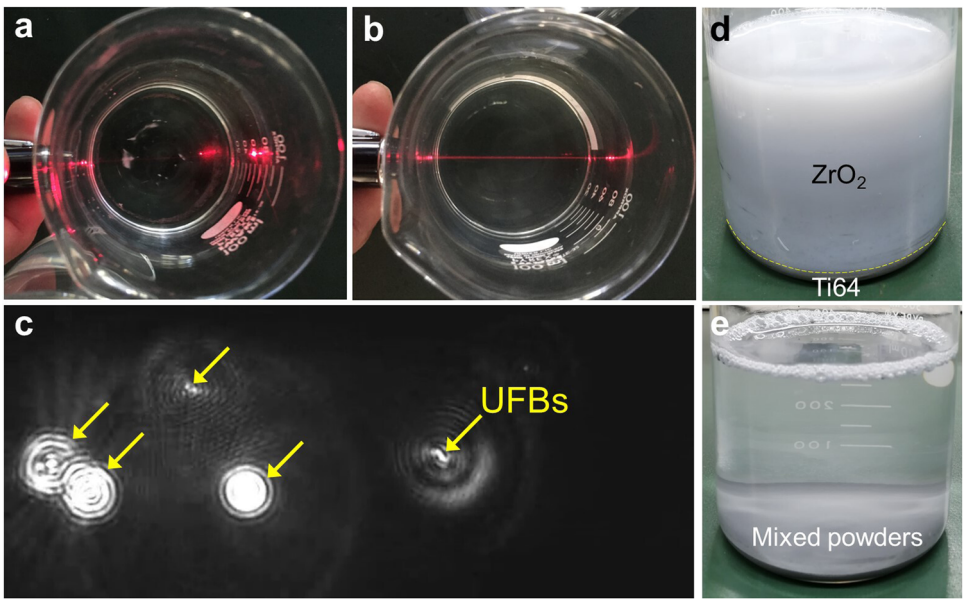

Fig. 2 Characteristics of the UFBs water and the mixed suspensions by heteroagglomeration. Photographs of a red laser beam passing through **a** deionized and **b** UFB water. **c** Snapshot of scattered light by UFBs. Photographs of a 5 wt% ZrO_2/Ti64 suspension produced in **d** deionized and **e** UFB water after settling for 5 and 0.5 h, respectively. Insert in **d** shows the sedimented Ti64 powders in the beaker after removing the supernatant.

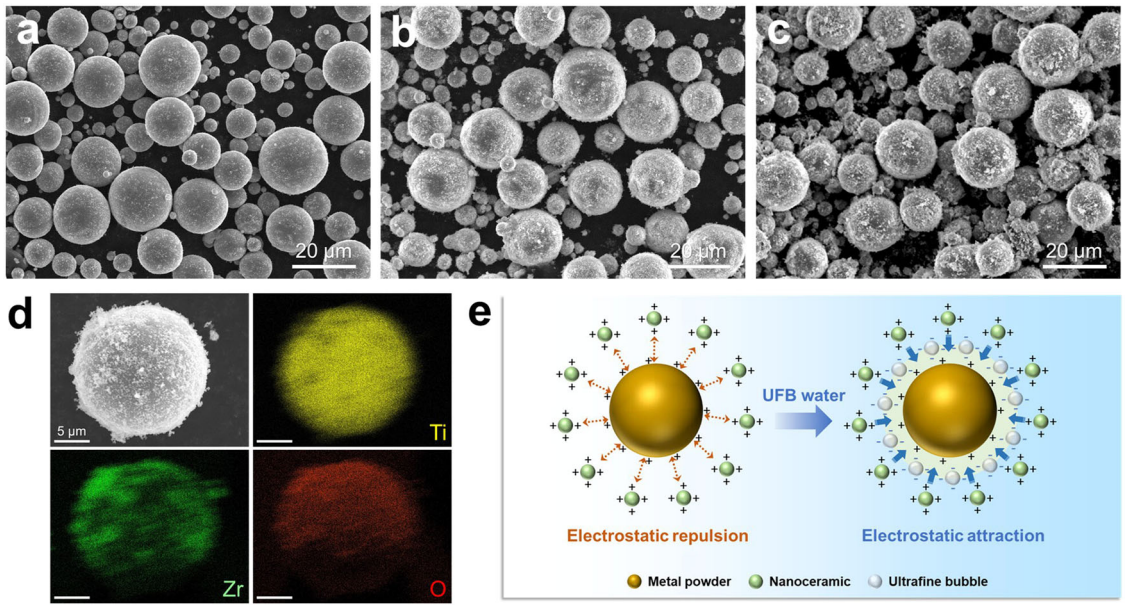

Fig. 3 Morphology of UFBH-processed nanoceramic/Ti64 powders and schematic illustration of the UFBH process. FESEM images of **a** 1 wt %, **b** 5 wt%, and **c** 10 wt% ZrO_2/Ti64 powders. **d** FESEM image and corresponding EDXS mappings of the 10 wt% ZrO_2/Ti64 powders. **e** Schematic illustration of the UFBH process.

the Ti64 particle was occupied with the addition of 10 wt% ZrO_2 nanoparticles (Fig. 3c, d). A similar tendency was also observed during the preparation of Al_2O_3/Ti64 mixed powders (Fig. S2).

To quantitively clarify the effect of UFBs, a series of ZrO_2/Ti64 and Al_2O_3/Ti64 mixed powders were prepared using different amounts of UFB water with 10 wt% nanoparticle addition (see Fig. S3). With increasing UFB water content, the number of ZrO_2 particles decorated on the powder surface gradually increased and subsequently saturated at approximately 9.6 wt% in the obtained composite powders, possibly owing to the limited surface area of the Ti64 powders. A similar tendency was also observed in the UFBH process of Al_2O_3/Ti64 powders with a maximum Al_2O_3 decoration of ~9.7 wt% in the obtained composite powders (Fig. S3).

The movement of nanoparticles during the hetero-agglomeration process was monitored in situ using a high-magnification optical microscope. In the deionized-water-based suspension, the ZrO_2 nanoparticles hardly approached the Ti64 powders due to their electrostatic repulsion (Movie S1). In contrast, the ZrO_2 nanoparticles gradually attached to the surface of Ti64 powders using UFB water (Movie S2). Correspondingly, the principle of UFBH is schematically proposed in Fig. 3e. The negatively charged UFBs served as an expected bridging agent between the positively charged metal and nanoceramic powders for uniform dispersion. UFBs subsequently burst during the drying process, while the nanoceramics were tightly attached to the metal powder surface under van der Waals forces. Furthermore, the dispersion of nanoceramic/Ti64 powders remained uniform after five cycles of L-PBF-based recoating (Fig. S4), confirming the formation of a strong bond between the nanoceramic and metal powders.

There was a significant trade-off between the dispersion and flowability of composite powders prepared via commonly used ball milling. In contrast, the uniform 5 wt% ZrO_2/Ti64 powders displayed a lower avalanche angle of 45.4° than the Ti64 powder (49.6°), indicative of enhanced flowability upon nanoceramic decoration. This result was likely attributed to the unchanged powder morphology as well as the increased surface roughness, resulting in decreased van der Waals forces among metal particles[23].

Although the ceramic nanoparticles exhibited a laser absorptivity of <30%, the 1070 nm (laser wavelength utilized in L-PBF) laser absorptivity of the Ti64 powder (74.0%) remained high after being decorated with 10 wt% ZrO_2 (75.0%) and Al_2O_3 (74.9%), as shown in Fig. S5. This enhancement of absorptivity was attributed to the occurrence of multiple laser reflections induced by the surface protruded nanoceramics. Thus, the AM properties of metal powders were simultaneously enhanced upon nanoceramic decoration.

Microstructures and mechanical properties of nanoceramic/Ti64 builds

To verify the AM processability of nanoceramic-decorated metallic powders, the representative 1 wt% ZrO_2/Ti64 powders were subjected to the L-PBF process. A fully dense composite build was fabricated using optimum building

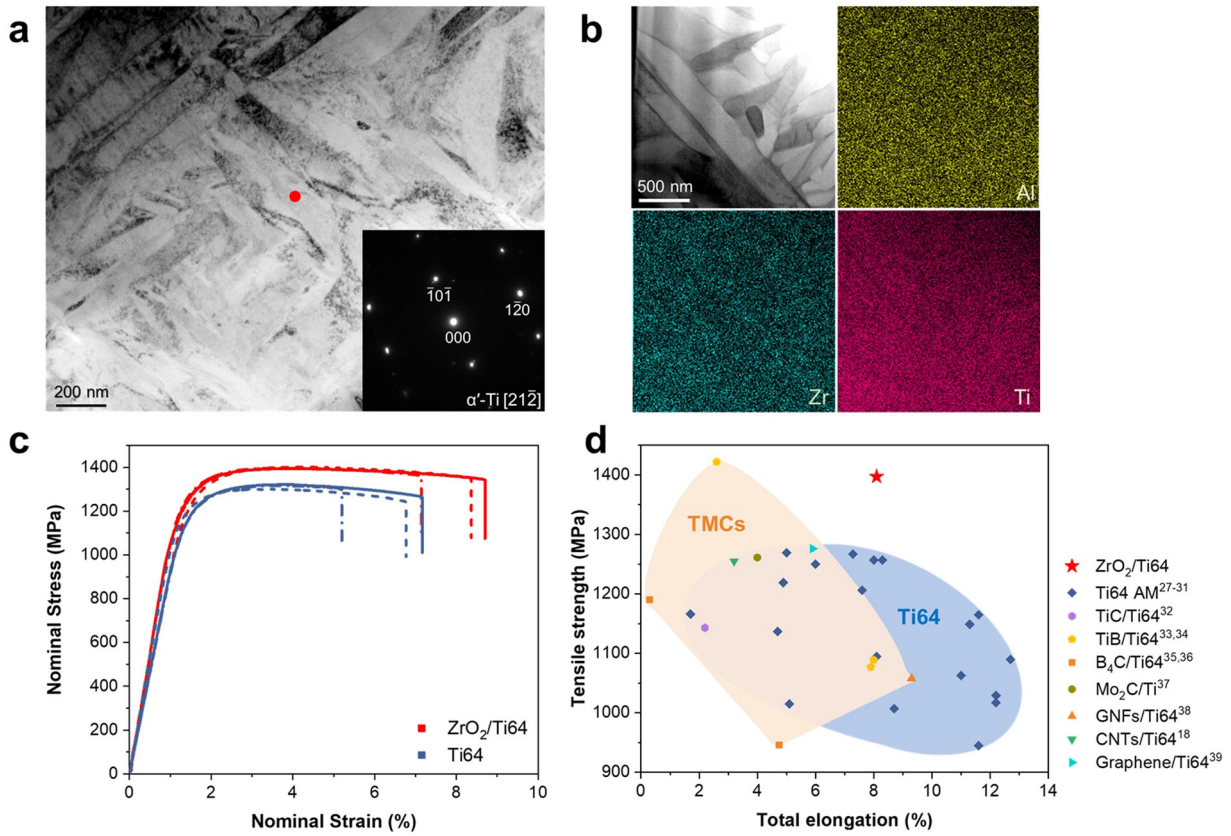

Fig. 4 Characteristics of nanoceramic/Ti64 builds prepared by UFBH process. a TEM image, **b** STEM image, and the corresponding EDXS mappings of the ZrO_2/Ti64 composite build. **c** Nominal stress–strain diagrams of the L-PBF-processed Ti64 alloy and 1 wt% ZrO_2/Ti64 composite. **d** Tensile strength as a function of elongation of the composite build as compared with previously reported Ti-based materials. Insert in **a** shows the SAED pattern of α′-Ti taken from the red spot.

parameters, which are detailed in the Methods section. As illustrated by the FESEM image in Fig. S6 and TEM/STEM images in Fig. 4a, b, the composite build was composed of fine α′-Ti martensite owing to the high solidification rate of 10^3–10^8 K/s[24]. No ceramic phases were detected in the build, indicating that the ZrO_2 nanoparticles completely decomposed and dissolved into the matrix upon laser irradiation.

All elements were homogeneously distributed in the build without noticeable macrosegregation (Fig. 4b) owing to the thermally dynamic and nonequilibrium nature of the L-PBF process and the powder homogeneity induced by UFBH. This unique structure has rarely been reported in 3D-printed composites because aggregated nanofillers are difficult to fuse[11,25]. In addition, the size of the α′-Ti martensite grains decreased with increasing nanoceramic content. This occurred because foreign solution atoms, such as oxygen, acted as nucleating sites and hindered the growth of grains during the solidification process, contributing to grain refinement[26].

The mechanical responses of the L-PBF build were measured by standard tensile tests. Figure 4c displays the nominal tensile strain–stress diagrams of the Ti64 alloy builds and 1 wt% ZrO_2/Ti64 composite builds. The average yield strength (YS), ultimate tensile strength (UTS), and total elongation of the Ti64 alloy builds were determined to be 1167 ± 2 MPa, 1312 ± 9 MPa, and 6.4% ± 0.8%, respectively. Moreover, the YS, UTS, and total elongation of the 1 wt% ZrO_2/Ti64 composite were measured as 1210 ± 16 MPa, 1397 ± 3 MPa, and 8.1% ± 0.7%, respectively, exhibiting a simultaneous enhancement of strength and ductility through nanoceramic incorporation. Correspondingly, the composite material underwent ductile fracture behavior characterized by fine dimples evenly distributed over the tensile fracture surfaces (Fig. S7). More importantly, the 1 wt% ZrO_2/Ti64 build showed an outstanding balance of high strength and acceptable ductility in relation to the commonly used Ti64 alloy components and novel AM-produced Ti matrix composites[18,27–39] (Fig. 4d).

The unique effects of UFB were further confirmed by comparing the mechanical properties of L-PBF builds using composite powders prepared with UFB or deionized water during the heteroagglomeration process. Fig. S8 displays the

tensile strain–stress curves of the 0.5 wt% Al_2O_3/Ti64 build using UFB water, as well as the 1 wt% ZrO_2/Ti64 and the 1 wt% Al_2O_3/Ti64 builds using deionized water. The corresponding tensile properties of the L-PBF builds are summarized in Table S1. The mechanical properties of both the 1 wt% ZrO_2/Ti64 and the 1 wt% Al_2O_3/Ti64 builds using deionized water showed no insignificant difference compared to those of the Ti64 builds. However, the 0.5 wt% Al_2O_3/Ti64 build using UFB water possessed a high UTS of 1634 ± 5 MPa and an acceptable total elongation of 3.7% ± 0.1%. The results confirmed that the use of UFB played a critical role in improving the dispersion of nanoceramic particles and the mechanical performance of the final L-PBF builds.

Figure S9 shows the typical microstructure of a ZrO_2/Ti64 sample using UFBH near the fracture surface after tensile testing. Compared with the microstructure of the as-printed sample in Fig. 4a, a higher density of dislocations was observed throughout the martensite structures, especially near the grain boundaries (see red arrows in Fig. S8). This result confirmed that the martensite grain boundaries had significant pinning effects on the dislocation movement during the deformation process. Consequently, the superior properties of L-PBF composites were attributed to the grain refinement effect and solid-solution strengthening during laser AM of the unique nanoceramic-decorated metal powders. The strengthening contributions of the two factors were theoretically calculated (see Supplementary Note 2) and are shown in Fig. S10. Notably, the calculated YS values of the L-PBF builds were consistent with the experimental values.

Conclusions

In summary, a novel UFBH method was proposed to economically fabricate high-concentration, impurity-free nanoceramic/metal powders for AM. The negatively charged UFBs promoted the uniform decoration of the positively charged nanoceramic particles on the metal powder surface via electrostatic self-assembly. Thus, individual ZrO_2 or Al_2O_3 nanoparticles up to 10 wt% were tightly attached to Ti64 particles without a change in their initial size or shape. Due to the increased surface roughness of the protruding nanoceramics, the laser absorptivity and flowability of the Ti64 powders improved, resulting in enhanced AM processability. Subsequently, a dense 1 wt% ZrO_2/Ti64 component was successfully fabricated by the L-PBF process. The TEM results showed that the ZrO_2 nanoparticles underwent a typical decomposition/dissolution process upon laser irradiation. Owing to the significant solid solution strengthening and grain refinement, a unique composite with a high UTS of 1.4 GPa and a high elongation of 8.1% was obtained; these values were higher than those of conventional Ti-based materials. This study promotes the production of novel composite powders and high-performance AM components.

Materials and methods

Materials

Commercially available ZrO_2 (Tosoh Co. Ltd., Japan) and Al_2O_3 nanoparticles (Taimei Chemicals, Japan) with a purity of >99.9% were used as ceramic fillers. Gas-atomized Ti64 powder with D_{10}, D_{50}, and D_{90} values of 5.7, 14.0, and 22.2 μm, respectively, was supplied by AP&C Inc., Canada. An in-house-developed decompression-type UFB generator was used for UFB water preparation. The machine introduces high-pressure gas into the water through a nozzle to generate UFBs[40]. UFB water was then fabricated using air and 20 L of deionized water.

Fabrication of nanoceramic-decorated metal powders

The nanoceramic/Ti64 powders were prepared by a heteroagglomeration process as follows. First, 0.3, 1.5, or 3 g of ZrO_2 (or Al_2O_3) nanoparticles and 29.7, 28.5, or 27 g of Ti64 powders were separately dispersed in 200 mL of deionized water with ultrasonication and mechanical stirring in an ice-water bath for 1 h. Subsequently, the ZrO_2 or Al_2O_3 colloid was added slowly into the Ti64 suspension via mechanical blending. Then, 1 L of UFB water was added dropwise into the suspension mixture, followed by mechanical stirring for 0.5 h. After settling for 0.5 h, the mixed powders containing 1, 5, and 10 wt% nanoceramic were obtained by filtration through filter paper (No. 101, Advantec, Japan) and vacuum-drying at 298 K. For comparison, 1 wt% ZrO_2/Ti64 and 1 wt% Al_2O_3/Ti64 powders were prepared using the same heteroagglomeration process by changing UFB water to deionized water.

L-PBF processing

The Ti64 alloy, ZrO_2/Ti64 and Al_2O_3/Ti64 composite bulks were produced using an L-PBF machine (Concept Laser MlabR, Germany) equipped with a Yb fiber laser system (laser wavelength 1070 nm). All L-PBF builds were fabricated with a laser power of 95 W, a scanning speed of 800 mm·s^{-1}, a hatch distance of 90 μm, and a layer thickness of 25 μm. The building process was conducted under a high-purity argon atmosphere with a low oxygen concentration (<0.1%). The L-PBF builds had a rectangular shape with width, length, and height of 6 mm, 30 mm, and 6 mm, respectively.

Characterizations

The zeta potential of ZrO_2, Al_2O_3 nanoparticles, and UFB water was determined using a nanoparticle analyzer (ELSZ-2000, Otsuka, Japan). The characterization of UFBs was conducted using a Nanosight NS300 system (Malvern Instruments, UK) equipped with a 405-nm laser light source and a sCMOS camera. The obtained data were

analyzed using Nanoparticle Tracking Analysis software (version 3.4). The observation of suspension movement during the UFBH process was conducted using an optical microscope (BX51, Olympus, Japan) equipped with cellSens Standard imaging software (version 1.5). The microstructure observation of the powders and L-PBF builds was performed through FESEM (JSM-6500F, JEOL, Japan), HRTEM (HF-2000EDX, Hitachi, Japan), and STEM (JEM-ARM200F, JEOL, Japan). The electron microscopy specimens were prepared by using a focused ion beam system (JIB-4600F, JEOL, Japan). The oxygen concentrations of the powders and L-PBF builds were determined by combustion analysis (ONH836, LECO Co., Ltd., USA).

Mechanical properties

The dog-bone-shaped specimens were prepared from the L-PBF builds using an electric discharge machine for the tensile tests. The width, length, and height of the gauge section of the tensile samples were 2 mm, 10 mm, and 1.8 mm, respectively. All specimens were polished with SiC emery papers until the surface roughness was <40 μm. Uniaxial tensile tests were conducted on a universal testing machine (INSTRON 5892, US) at room temperature with an initial strain rate of $1 \times 10^{-3}\,s^{-1}$. The tensile direction of all specimens was perpendicular to the building direction of the L-PBF process. Digital image correlation (DIC) technology was performed with camera recording (EF-X1, Casio, Japan) during the tensile tests. The obtained data were analyzed using Strain Analysis software (DIPP-Strain, DITECT, Japan). To improve the measurement accuracy, the elastic strain was also detected using foil strain gauges (KFGS-4N-120-C1-11, KYOWA, Japan) that were attached to the surface of the specimens. Both the Ti64 and ZrO_2/Ti64 builds were tested three times. The 0.2% offset YS, UTS, and total elongation were obtained from the stress versus strain curves.

Acknowledgements

The authors would like to thank Dr. Yoshimi Sato, Aqua Solutions Co., Ltd., Tsuruoka, Japan, for UFB water preparation. The authors would also like to thank Dr. Zhenxing Zhou for his assistance with the UFB water preparation. We acknowledge Dr. Kosei Kobayashi and Dr. Takamichi Miyazaki for their assistance with the TEM analysis. M. D. acknowledges the support by the Japan Society for the Promotion of Science (JSPS) KAKENHI Grant Number JP22KJ0322.

Author contributions

M.D. and W.Z. conceived the idea and designed the experiments. M.D. and S.G. prepared the UFB water and characterized the nanoparticles. M.D. fabricated the composite powders by the UFBH process and carried out the L-PBF process. M.D., W.Z. and S.G. conducted the characterization of composite powders and L-PBF builds. M.D., W.Z. and N.N. wrote the article with contributions from all authors. N.N. supervised the whole work.

Data availability

The data that support the findings of this study are available from the corresponding author upon reasonable request.

Conflict of interest

M.D., W.Z. and N.N. are inventors on a patent application related to this work filed by Tohoku University (No. P20200385-01, filed on 5 September 2022). The remaining authors declare no competing interests.

Publisher's note

Supplementary information The online version contains supplementary material available at https://doi.org/10.1038/s41427-023-00494-9.

Received: 28 February 2023 Revised: 20 July 2023 Accepted: 28 July 2023.
Published online: 8 September 2023

References

1. Raabe, D., Tasan, C. C. & Olivetti, E. A. Strategies for improving the sustainability of structural metals. *Nature* **575**, 64–74 (2019).
2. Lu, K. The future of metals. *Science* **328**, 319–320 (2010).
3. Martin, A. A. et al. Dynamics of pore formation during laser powder bed fusion additive manufacturing. *Nat. Commun.* **10**, 1–10 (2019).
4. Gu, D. et al. Material-structure-performance integrated laser-metal additive manufacturing. *Science* **372**, eabg1487 (2021).
5. Chen, L.-Y. et al. Processing and properties of magnesium containing a dense uniform dispersion of nanoparticles. *Nature* **528**, 539–543 (2015).
6. Krakhmalev, P. & Yadroitsev, I. Microstructure and properties of intermetallic composite coatings fabricated by selective laser melting of Ti–SiC powder mixtures. *Intermetallics* **46**, 147–155 (2014).
7. Gu, D., Hagedorn, Y.-C., Meiners, W., WisseUFBach, K. & Poprawe, R. Nanocrystalline TiC reinforced Ti matrix bulk-form nanocomposites by selective laser melting (SLM): densification, growth mechanism and wear behavior. *Compos. Sci. Technol.* **71**, 1612–1620 (2011).
8. Attar, H. et al. Comparative study of microstructures and mechanical properties of in situ Ti–TiB composites produced by selective laser melting, powder metallurgy, and casting technologies. *J. Mater. Res.* **29**, 1941–1950 (2014).
9. Yi, M. et al. Comparative investigation on microstructures and mechanical properties of (TiB+ TiC)/Ti-6Al-4V composites from Ti-B_4C-C and Ti-TiB_2-TiC systems. *Mater. Charact.* **140**, 281–289 (2018).
10. Ma, C., Chen, L., Cao, C. & Li, X. Nanoparticle-induced unusual melting and solidification behaviours of metals. *Nat. Commun.* **8**, 1–7 (2017).
11. Hattal, A. et al. Effect of nano-yttria stabilized zirconia addition on the microstructure and mechanical properties of Ti6Al4V parts manufactured by selective laser melting. *Mater. Des.* **180**, 107909 (2019).
12. Yan, Q., Chen, B. & Li, J. Super-high-strength graphene/titanium composites fabricated by selective laser melting. *Carbon* **174**, 451–462 (2021).
13. Shi, J. & Wang, Y. Development of metal matrix composites by laser-assisted additive manufacturing technologies: a review. *J. Mater. Sci.* **55**, 9883–9917 (2020).
14. Gu, D., Wang, H. & Zhang, G. Selective laser melting additive manufacturing of Ti-based nanocomposites: the role of nanopowder. *Metall. Mater. Trans. A* **45**, 464–476 (2014).
15. Reinhart, A., Ansell, T., Smith, W. & Nieto, A. Oxide reinforced Ti64 composites processed by selective laser melting. *J. Mater. Eng. Perform.* **30**, 6949–6960 (2021).
16. Tang, S. et al. Additive manufacturing of aluminum-based metal matrix composites—a review. *Adv. Eng. Mater.* **23**, 2100053 (2021).
17. Zhou, W. et al. Carbon nanotubes as a unique agent to fabricate nano-ceramic/metal composite powders for additive manufacturing. *Mater. Des.* **137**, 276–285 (2018).
18. Liu, Y., Li, S., Misra, R., Geng, K. & Yang, Y. Planting carbon nanotubes within Ti-6Al-4V to make high-quality composite powders for 3D printing high-performance Ti-6Al-4V matrix composites. *Scr. Mater.* **183**, 6–11 (2020).
19. Lin, T.-C. et al. Aluminum with dispersed nanoparticles by laser additive manufacturing. *Nat. Commun.* **10**, 1–9 (2019).

20. Bui, T. T., Nguyen, D. C. & Han, M. Average size and zeta potential of nanobubbles in different reagent solutions. *J. Nanopart. Res.* **21**, 173 (2019).
21. Najafi, A. S., Drelich, J., Yeung, A., Xu, Z. & Masliyah, J. A novel method of measuring electrophoretic mobility of gas bubbles. *J. Colloid Interface Sci.* **308**, 344–350 (2007).
22. Holmberg, J. P., Ahlberg, E., Bergenholtz, J., Hassellöv, M. & Abbas, Z. Surface charge and interfacial potential of titanium dioxide nanoparticles: experimental and theoretical investigations. *J. Colloid Interface Sci.* **407**, 168–176 (2013).
23. Lüddecke, A., Pannitz, O., Zetzener, H., Sehrt, J. & Kwade, A. Powder properties and flowability measurements of tailored nanocomposites for powder bed fusion applications. *Mater. Des.* **202**, 109536 (2021).
24. Khorasani, A. M., Gibson, I., Goldberg, M. & Littlefair, G. A survey on mechanisms and critical parameters on solidification of selective laser melting during fabrication of Ti-6Al-4V prosthetic acetabular cup. *Mater. Des.* **103**, 348–355 (2016).
25. Attar, H., Ehtemam-Haghighi, S., Kent, D. & Dargusch, M. S. Recent developments and opportunities in additive manufacturing of titanium-based matrix composites: a review. *Int. J. Mach. Tools Manuf.* **133**, 85–102 (2018).
26. Kondoh, K. et al. Tensile property enhancement by oxygen solutes in selectively laser melted titanium materials fabricated from pre-mixed pure Ti and TiO_2 powder. *Mater. Sci. Eng. A* **795**, 139983 (2020).
27. Carroll, B. E., Palmer, T. A. & Beese, A. M. Anisotropic tensile behavior of Ti–6Al–4V components fabricated with directed energy deposition additive manufacturing. *Acta Mater.* **87**, 309–320 (2015).
28. Jamshidi, P. et al. Selective laser melting of Ti-6Al-4V: the impact of post-processing on the tensile, fatigue and biological properties for medical implant applications. *Materials* **13**, 2813 (2020).
29. Li, P. et al. Coupling effects of high magnetic field and annealing on the microstructure evolution and mechanical properties of additive manufactured Ti–6Al–4V. *Mater. Sci. Eng. A* **824**, 141815 (2021).
30. Todaro, C. J. et al. Grain structure control during metal 3D printing by high-intensity ultrasound. *Nat. Commun.* **11**, 1–9 (2020).
31. Xu, W., Lui, E. W., Pateras, A., Qian, M. & Brandt, M. In situ tailoring microstructure in additively manufactured Ti-6Al-4V for superior mechanical performance. *Acta Mater.* **125**, 390–400 (2017).
32. Borisov, E., Masaylo, D. V. & Popovich, V. Selective laser melting of nanocomposite Ti-6Al-4V and TiC powder. In *Key Engineering Materials*. (Trans Tech Publ., 2019).
33. Yang, Z. W. et al. Balance of strength and plasticity of additive manufactured Ti-6Al-4V alloy by forming TiB whiskers with cyclic gradient distribution. *Addit. Manuf.* **39**, 101883 (2021).
34. Zhou, Z., Liu, Y., Liu, X., Zhan, Q. & Wang, K. Microstructure evolution and mechanical properties of in-situ Ti6Al4V–TiB composites manufactured by selective laser melting. *Compos. B Eng.* **207**, 108567 (2021).
35. Han, C. et al. Microstructure and mechanical properties of (TiB+ TiC)/Ti composites fabricated in situ via selective laser melting of Ti and B4C powders. *Addit. Manuf.* **36**, 101466 (2020).
36. Pouzet, S. et al. Additive layer manufacturing of titanium matrix composites using the direct metal deposition laser process. *Mater. Sci. Eng. A* **677**, 171–181 (2016).
37. Dadbakhsh, S. et al. Heat treatment possibilities for an in situ βTi-TiC composite made by laser powder bed fusion. *Addit. Manuf.* **36**, 101577 (2020).
38. Cao, Z. et al. Reinforcement with graphene nanoflakes in titanium matrix composites. *J. Alloy. Compd.* **696**, 498–502 (2017).
39. Lin, K. et al. Selective laser melting of graphene reinforced titanium matrix composites: Powder preparation and its formability. *Adv. Powder Technol.* **32**, 1426–1437 (2021).
40. Ikeura, H., Kobayashi, F. & Tamaki, M. Removal of residual pesticide, fenitrothion, in vegetables by using ozone microbubbles generated by different methods. *J. Food Eng.* **103**, 345–349 (2011).